Fuel 324 (2022) 124522

Contents lists available at ScienceDirect

Fuel

journal homepage: www.elsevier.com/locate/fuel

Full Length Article

Compressional wave phase velocity measurements during hydrate growth in partially and fully water saturated sandstone

M.M. Sæther *, S. Almenningen, G. Ersland, P. Lunde

University of Bergen, Department of Physics and Technology, Bergen, Norway

ARTICLE INFO

Keywords:
Hydrate-bearing sandstone
Compressional wave velocity measurements
Hydrate formation

ABSTRACT

The compressional wave phase velocity (c_P) has been measured as a function of hydrate saturation (S_H) during hydrate growth in Bentheim sandstone. The Fourier spectrum signal processing technique was used to specifically obtain the phase velocity at frequency 500 kHz. Eight experiments were conducted on eight Bentheim sandstone samples, having initial water saturation (S_{wi}) in the range 0.51–1. Based on the measurements, it is discussed how S_{wi} might affect the hydrate formation pattern during hydrate growth. For the sample having $S_{wi} = 0.51$, a clear increase is observed in the measured c_P from the beginning of the hydrate formation process. In the literature, micropore models ascribe such an increase to hydrates partly forming in soft, low aspect-ratio pores. For the samples having $S_{wi} \geq 0.68$, there is an initial stage in the hydrate formation process with little or no change in the measured c_P. The S_H interval defining this first stage seems to increase for increasing S_{wi}. As S_H further increase, a second stage follows where c_P increases. This is explained with hydrates first forming as a hydrate-water slurry before eventually solidifying and taking part of the solid frame. The results aid in understanding how the elastic properties of hydrate-bearing porous rocks change with S_H and S_{wi}.

1. Introduction

Vast quantities of methane gas hydrates stretch over large volumes beneath the ocean-bed, inland seas, and in the permafrost, and may potentially become an energy source [1,2]. In hydrate-bearing sediments, the hydrate saturation (S_H) may typically be related to the compressional (c_P) [2–15] and shear (c_S) wave velocities [2,3,6–8,12,13], and the compressional (α_P) and shear (α_S) wave attenuation coefficients [2,7,9]. Thus, acoustic methods have been pointed to as candidates for remote detection and monitoring of hydrate deposits [1,2].

In addition to S_H, and confining pressure, the acoustic parameters c_P, c_S, α_P, and α_S of hydrate-bearing poroelastic solid media depend on many other factors. The pore fluid, which is typically described with the gas (S_g) and water (S_w) saturations clearly affect c_P and c_S along with sediment composition in standard rock physics models such as Gassmann's equation [16]. The measurement frequency will affect all the acoustic parameters due to dispersion and attenuation mechanisms [15,17], and from laboratory studies the hydrate morphology is reported to have a clear effect on c_P and c_S [4–6,8,11–13]. Information on how these listed factors affect the acoustic parameters are needed to understand acoustic field measurements [2,3,7,18].

By interpreting the measured c_P and c_S using numerical models it has been investigated whether hydrates form primarily within the pore fluid, or hydrates take part in the solid frame. For unconsolidated sediments, numerical models distinguish between hydrates acting as load bearing grains [19] or as cement in between the grains [20]. Cementing hydrates greatly affects c_P. Hydrates acting as load bearing grains and hydrates forming in the pore fluid has some effect, and little or no effect, respectively, on c_P.

The differential effective medium model (DEM) is regarded as suitable for modeling c_P in consolidated sandstones. In this model, hydrates take part in the solid frame by filling up the pores which is described with spheroids having different aspect ratios [16]. Cementing effects in sandstones are typically regarded as solid material filling up the low aspect ratio pores [22].

Zhang et al. [11] studied the hydrate morphology during hydrate growth in unconsolidated sand for a range of initial water saturations (approximately 0.15 – 0.70). Hydrate forming in the samples in the lower water saturation range, was reported to mainly act as cement between the grains. For samples in the intermediate to high water saturation range, a combination of all three hydrate morphology

* Corresponding author.
E-mail address: mathias.sather@uib.no (M.M. Sæther).

https://doi.org/10.1016/j.fuel.2022.124522
Received 14 January 2022; Received in revised form 12 April 2022; Accepted 3 May 2022
Available online 14 May 2022

scenarios was used to describe the change in c_P during hydrate growth. Hydrate tended to form, primarily within the pore fluid early in the hydrate formation process, S_H typically less than 0.1, and act as load bearing grains for S_H typically in the range of 0.1 – 0.2, and act as cement for S_H typically higher than 0.2.

In a study by Hu et al. [8], an artificial consolidated porous ceramic material having $S_{wi} = 1.0$ and baseline compressional wave velocity (c_P at $S_H = 0$) approximately 4250 m/s, was subject to methane hydrate growth. Hydrates were reported to, form in the pore fluid for S_H less than 0.3 and, form as part of the solid frame for $S_H > 0.3$.

Sadeq et al. [23] formed synthetic hydrate (THF) in Bentheim sandstones. The samples were initially fully saturated with a solution of 15 % THF and 85% water. c_P was measured as a function of time and reported to increase from approximately 3450 m/s at baseline condition to 3850 m/s at maximum hydrate saturation. A confining pressure of 14 Mpa was used. The measured c_P was observed to not change at the start of the hydrate formation process. It was argued that this was due to hydrates forming in the pore fluid.

Both sonic (typically less than 30 kHz) [6,9] and ultrasonic frequencies (typically higher than 100 kHz) [4,5,8,10,11,13] have been used to study elastic wave velocities in methane hydrate bearing sediments in the laboratory. As pointed out by Priest et al. [6], for hydrate-bearing sediments, elastic velocity measurements using ultrasonic frequencies are typically higher compared with those obtained from seismic data due dispersion mechanisms. Theoretical models considering Biot flow and acoustic scattering in hydrate bearing sediments have been developed to understand dispersion mechanisms for a wide range of frequencies [15,17]. To use such models the specific measurement frequency must be specified, which is typically not done in studies where ultrasonic frequencies have been used [4,5,8,10,11,13].

In studies where ultrasonic measurement frequencies have been used, c_P and c_S have traditionally been obtained by measuring the transit time of the first arrival of the acoustic pulse transmitted through the hydrate-bearing samples [4,5,8,10,11,13]. The accuracy of this measurement method has been debated in e.g [24], especially for use with porous media. In this study it is argued that the first arrival of the signal may be partly buried in noise, and for very high attenuation the whole first cycle may be difficult to detect. In addition, the frequency content of the transient of the signal is not defined, therefore, measurements of wave velocities using the first arrival of the signal must be regarded as a measure of the group velocity, and not the phase velocity [24]. To overcome such challenges, the Fourier spectrum signal processing method [25] may be used to measure the compressional wave phase velocity. Using the Fourier method, any recording of a finite pulse is a measure of the average properties of the medium in which the pulse travels through. Due to the defined frequency, measurements using this method may also provide valuable data for verification of numerical models considering dispersion.

To interpret seismic field data from hydrate-bearing sediments, the hydrate morphology and it's relation to c_P is a key area of interest. To aid in understanding this relation, unconsolidated sand-pack samples have been used to facilitate hydrates [4–6,11,26–28], and to represent hydrate-bearing sediments occurring in the nature. In several studies, consolidated porous media have also been used to facilitate methane hydrates [8,12] and synthetic hydrates (tetrahydrofuran, THF) [23,29,30] to aid in understanding how c_P is affected by complex mechanisms in hydrate bearing reservoirs. Potential grain migration during hydrate growth [31] may also pose an increased level of complexity when using unconsolidated sand as the host sediment. By using a rigid consolidated sandstone with a relatively uniform pore size distribution, such as Bentheim sandstone, the complexity of the measurement system may be reduced. In the current work, Bentheim sandstone was used as the host sediment. Due to the uniformity of the sandstones, different cores are assumed to be comparable in terms of measured c_P for the same initial conditions, such as initial water saturation, S_{wi}.

There are quite a few laboratory studies on the acoustic properties of hydrate bearing sediments, e.g. [4–6,8,10–13,23,26–30]. Few of these mentioned studies report measurements of c_P during hydrate growth over a wide initial water saturation (S_{wi}) range [11,26]. As pointed out in [26], more published data will aid in understanding the complex mechanisms in hydrate bearing reservoirs, and also provide valuable input parameters to numerical models aiming to relate e.g. c_P and S_H.

The objective of the present work is to study the relation between hydrate growth pattern and phase velocity, c_P, in Bentheim sandstone for initial water saturation, S_{wi}, over a wide range, 0.51 – 1. A consolidated sandstone was used as host material to reduce the complexity compared with a typical unconsolidated hydrate bearing system found in nature, where e.g. grain migration during hydrate growth might occur [31]. In particular, the aim is to relate the sole impact of hydrate growth on c_P to the hydrate growth pattern for S_{wi} in the range 0.51 – 1. The Fourier spectrum signal processing method is used to obtain the phase velocity c_P at 500 kHz.

2. Sample preparation and experimental procedure

2.1. Sample preparation

Hydrates were formed in the pore space of a high porosity, highly permeable sandstone acquired from the Bentheim quarry in Lower Saxony, Germany. The Bentheim sample used in these experiments had a porosity (β_0) of approximately 23% and a permeability of 1–2 D, and was characterized by uniform pore geometry with an average pore diameter of 125 μm. This outcrop rock has been characterized by 95.5 % quartz, 2.0% kaolinite, 1.7% K-feldspar, and 0.8% other [32]. Bentheim sandstone has very low clay content [33] and no clay swelling has been observed in the current work. Eight individual cylindrical core plugs cut from the same batch were prepared with diameter 50.8 mm and different lengths (L) (Table 1). The core plugs were dried at 70 °C for 24 h to remove all moisture and the dry weight was recorded. Each core plug was saturated with a given amount of water by one of two different methods [35,38]. In method (i), the dry core plugs were submerged in water for some time to allow water to invade the pore space by spontaneous imbibition at ambient conditions. The submerging time for the core in experiment 1 was 10 min; for experiments 2–3, two hours; for experiment 4–6, 24 h. In method (ii), the dry core plugs were first purged in a vacuum chamber (less than 1000 Pa) for two hours. The cores were then completely saturated by opening a valve to a secondary chamber containing water at ambient conditions. A standardized slightly saline water solution available at the laboratory facility was used as the water phase, containing distilled water with 0.1 wt% NaCl. Two of the core plugs were saturated by method ii), while the others were saturated by method i) (Table 1). The average initial water saturation, S_{wi} (S_w before hydrate growth), was calculated by the weight difference of the wet and dry core. Table 1 shows S_{wi}, saturation method, sample length (L), porosity, and figures giving the corresponding measurements.

The sensitivity of S_{wi} in the cores based on uncertainties in the

Table 1
The experiment numbers (Exp. No.) are listed from low to high S_{wi}, saturation method (cf. text), sample length (L), porosity, and figures giving the corresponding experimental results.

Exp. No.	S_{wi}	Saturation method	L [mm]	Porosity (β_0)	Figure
1	0.51	i)	44.4	0.233	Figs. 4 and 7
2	0.68	i)	48.7	0.239	Figs. 4 and 7
3	0.72	i)	49.2	0.237	Figs. 4 and 7
4	0.77	i)	48.4	0.239	Figs. 5 and 7
5	0.80	i)	42.7	0.239	Figs. 5 and 7
6	0.82	i)	42.4	0.237	Figs. 5 and 7
7	1.00	ii)	37.9	0.229	Figs. 6 and 7
8	1.00	ii)	53.7	0.229	Figs. 6 and 7

measured mass and pore volume of the sandstone, is found to be less than 0.02, which is in agreement with [34]. A note must be made for experiments 7–8 where S_{wi} is reported to be 1. Here water drainage near the surface of the sandstone will give an effectively smaller S_{wi}, however, in the core, S_{wi} is assumed to be unity. NMR imaging of similar Bentheim sandstone cores has previously shown that saturation method (i) gives local variations of the water saturation in the length direction of approximately 0.02, and in the inner parts of the sandstone, a radial variation of approximately 0.07 [35]. No systematic water congestion due to gravity is reported. Although there is some spatial variation in the water saturation, the Fourier spectrum method measures the average properties of the sandstone.

2.2. Pressure cell setup and hydrate formation procedure

The experimental system consists of the sandstone core sample, a Hassler core holder [34] (Fig. 1) to maintain the sample at high pressure and low temperature, a high pressure control system (overburden), and a pump to supply methane and control the pore pressure.

The transducers and buffers placed inside two transducer holders were pressed onto the sample by applying a 10 Nm torque using a 30 cm long torque wrench on the endpiece. By assuming frictionless endpiece threads, this torque will give an axial stress on the Bentheim sandstone of approximately 0.3 Mpa. A plexiglas cup, rubber ring, and centralizing ring were used to keep the transducers, buffers, and the sample aligned (see [36] for more details). All flow lines leading into the core were purged under vacuum and filled with methane gas. Using a Stigma pressure pump, the core plug was subsequently pressurized from both ends to 8.3 Mpa. The confinement pressure was continuously kept at 3.0 Mpa above the pore pressure by applying pressurized confining oil (11.3 Mpa) around the rubber sleeve (see Fig. 1). This results in a confinement stress of approximately 3 Mpa, much higher than the axial stress from the buffers. The core plug was pressurized at room temperature up to several days to allow methane to equilibrate with the water. Afterwards, the leakage rate of the system was determined for all experiments 1–8 by logging the Stigma pressure pump volume for 24 h. The leakage rates in experiments 1–8 were observed to be less than 0.04 mL/hour which are deemed small for these kinds of experiments [34].

A temperature bath controlled the coolant temperature, which in turn was transferred to a cooling jacket surrounding the core holder shown in Fig. 1. The pressure and temperature were controlled and monitored by computers, which allowed the test to run unattended for extended periods of time.

Hydrate formation was initiated by cooling – well below the methane hydrate formation temperature: 11.2 °C, at pressure 8.3 Mpa, and salinity 0.1 wt% NaCl, as calculated using the CSMGem software [37]. The temperature was reduced by flowing cooled antifreeze fluid through a cooling jacket that surrounded the core holder (not shown in Fig. 1). Following this formation procedure, NMR imaging shows that hydrate may be formed inside sandstone samples with S_{wi} up to unity [38]. In experiments 7–8, where S_{wi} is reported to be 1, methane invades inner

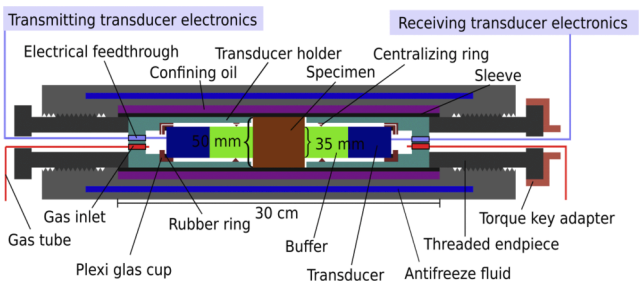

Fig. 1. Schematics of the pressure cell containing transducers, buffers, the hydrate-bearing sample, and other equipment needed for conducting acoustic and pressure cell regulation measurements.

pore spaces by dissolving into the water [38]. Hydrate formation from dissolved methane gas is a much more slow process than hydrate formation on the gas/water interface [39]. Thus, experiments 7–8 ($S_{wi} = 1$) lasted for weeks and experiments 1–6, where free gas was available, lasted up to a few days. For each experiment, acoustic waveforms were logged continuously.

The hydrate saturation, S_H, was quantified by the amount of methane gas consumed during hydrate growth assuming a hydration number of 5.99, and leakage rates were corrected for as described by [40]. Throughout the hydrate formation process the pore pressure was maintained at 8.3 Mpa by the pressure pump. For all experiments the consumed methane gas was logged on a computer communicating with the gas pressure pump. Loggings may be found in [41].

Numerous experiments have been conducted using the Hassler core holder shown in Fig. 1 [34,35,38,40]. In different Bentheim sandstone samples using this specific Hassler core holder, the uncertainty in S_H due to uncertainty contributions from the pressure pump methane volume, hydration number, methane gas density, thermometer precision, fluctuations of temperature in the pressure pump, and leakage rate is reported to be less than 0.02 [34]. This reported uncertainty in S_H for hydrate-bearing Bentheim sandstone samples inside the Hassler core holder applies for experiments with a low leakage rate [34] which is indeed the case for the current experiments with leakage rates less than 0.04 mL/hour. A relatively uniform hydrate distribution has been reported for experiments like this [38], although the spatial variation in the water saturation will affect the uniformity of hydrate saturation.

2.3. Acoustic experimental setup

c_P was measured using the buffer rod arrangement with the pulse-transmit acoustic measurement method [42]. Fig. 1 shows how transducers, buffers, and the specimen are fitted inside the pressure cell. The "transmitting electronics" in Fig. 1 are the equipment needed to generate the electric input signal for the transmitting transducer. This consist of an Agilent 33250A signal generator, an ENI 240L RF power amplifier, a 33 mH inductor, a Hatfield attenuator, and electrical cables. The attenuator was used to ensure and confirm that non-linear effects did not affect the measurements significantly. The 33 mH inductor was used as a simple impedance matching filter between the attenuator and the transmitting transducer. It was used to remove some of the reactance (imaginary part) of the impedance of the transmitted electrical signals.

"The receiving electronics" represents a Hewlet Packard signal amplifier, a Krohn-Hite 3202 bandpass filter, a 33 mH inductor used for impedance matching, a DPO 3000 Techtronix oscilloscope, and electrical cables. A computer was used to log the measured signals from the oscilloscope via USB connection, and to control the input settings on the signal generator via an IEEE 488 USB-GPIB adapter.

Two measurements are conducted when using the buffer rod method: Reference measurement A without the sample inserted (as shown in Fig. 1 without the sandstone), and measurement B with the hydrate bearing sample inserted into the wave propagation path (as shown in Fig. 1). Using the Fourier spectrum signal processing method, c_P is found by subtracting the phase of reference measurement A and measurement B. Doing this, time delays caused by the buffers, transducers, and other electric components in the measurements are automatically corrected for. The PC-controlled waveform input settings on the signal generator was a 1–2 cycles pulse, having center frequency 500 kHz and burst repetition rate 50 ms. The amplitude setting was dynamically changed as described in the experimental procedure below. A high-pass filter with a 200 kHz cut-off frequency was applied, to remove low frequency components. The oscilloscope acquired the signal by continuously averaging 256 measured signals. The acoustic waveform was logged every 15 min.

In the project funding this research, the idea was to measure both P and S-waves. P and S-wave transducers with center frequencies 530 and 460 kHz, respectively, were designed and build in-house to fit inside the

pressure cell. However, S-waves were heavily attenuated in the experiments and mode conversion between S and P-waves may hamper the direct shear wave pulse. Thus only P-wave measurements are reported in this work. In experiments 1–3, the P-wave transducers were used and in experiments 4–8 the P-waves generated by the S-wave transducers were used. For further details on the design and construction of these transducers, cf. [36].

In a test measurement where the transducers were face to face (measurement A), a distorted signal was seen on the oscilloscope due to non-linear effects. To avoid this, the attenuator setting was set to 20 dB attenuation. No phase response was observed for the attenuator. In experiments 1–8 (measurement B), non-linear effects were avoided by gradually decreasing the signal generator amplitude from 100 mV to 1 mV during the measurements.

2.4. Fourier spectrum signal processing technique

As pointed out in [43], the Fourier spectrum signal processing method [25] can be used in pulse-transmit measurements using the buffer rod arrangement to measure c_P for a porous rock. For precise ultrasonic measurements, the measured phase spectra should be corrected for diffraction effects [44]. By including the diffraction correction in the original method developed by [25], c_P has been obtained in this work with [36]

$$c_p = \frac{2\pi f L}{\angle V_{\mathrm{A}}(f) - \angle V_B(f) + \angle H_{\mathrm{B}}^{dif}(f) - \angle H_{\mathrm{A}}^{dif}(f)}, \tag{1}$$

where f is the frequency. $\angle V_A$ and $\angle V_B$ are the discrete Fourier transform phase spectra of the P-wave pulses in measurements A and B, respectively. $\angle H_A^{dif}$ and $\angle H_B^{dif}$ are the diffraction correction phase spectra for measurement A and B, respectively, where H_A^{dif} and H_B^{dif} are the diffraction corrections.

Typical examples of the time traces using the S-wave transducer for measurements A and B are shown in Fig. 2. The first event in the time traces, A_P and B_P, are the direct transmitted P-wave pulses, which are used in this work. A_S and B_S are the direct transmitted S-wave events. Not clearly visible in the figure, however, A_S and B_S may be hampered by the other surrounding reflected S and P-wave events. Thus, shear waves are not considered in this paper. t_{AP} and t_{BP} are defined 10 μs before the first peak in the pulse to ensure that potentially highly attenuated early signal components are included in the compressional wave event. Starting from t_{AP} and t_{BP}, the pulse is truncated after five cycles and zeropadded to a total signal length of 100,000 points (signal length 1 ms). The sampling frequency is 500 MHz and the frequency resolution of the Fourier spectrum is $\Delta f = 1$ kHz. The FFT – algorithm in MATLAB 2017 is used to calculate the discrete Fourier transform. Using this algorithm, the phase spectra are wrapped within -π and + π and phase jump discontinuities of 2π will be present. Such phase jumps have been corrected for by adding 2π at every discontinuity using the MATLAB 2017 function unwrap(). The Fourier spectrum signal processing technique is widely used for elastic velocity measurements, and more details on the method can be found in numerous studies, e.g [43]. A single event A_p or B_p (pulse) in Fig. 2 represents a wave with a wavefront covering (most of) the cross-section of the sample. Thus, the travel-time of the pulse gives information of the average properties of the sandstone, such as S_H. Thus, the Fourier method is suitable for measuring the average c_P in samples having some variation in properties such as hydrate and water saturation.

An expression derived by [45] has been used to calculate the diffraction correction for fluids and solids [46,47]. This approach has also been used in this work to calculate

$$\begin{aligned} H_A^{dif} &= 1 - e^{-i2\pi/Y_A}(J_0(2\pi/Y_A) + iJ_1(2\pi/Y_A)), \\ Y_A &= \frac{4\pi L_B}{k_b a^2}, \\ H_B^{dif} &= 1 - e^{-i2\pi/Y_B}(J_0(2\pi/Y_B) + iJ_1(2\pi/Y_B)), \\ Y_B &= \frac{4\pi L_B}{k_b a^2} + \frac{4\pi L}{k_m a^2}. \end{aligned} \tag{2}$$

Here, J_0 and J_1 are the first kind Bessel functions of the zeroth and first order, respectively and$i = \sqrt{-1}$. $k_b = \omega/c_P^b$ and $k_m = \omega/c_P$ are the compressional wave numbers in the buffer and the sample, respectively. c_P^b is the compressional wave velocity in the buffer and ω is the angular frequency. L_B is the of the buffer length. In this work, using P-wave transducers, Eq. (1) has been used with "a" equal to the piezoelectric element radius. For S-wave transducers, the piezoelectric elements are square shaped and a has been set to the radius of a circular disc with the same area as the square shaped element.

A rather thorough sensitivity analysis of uncertainty contributions in the measured c_P of experiments 1–8 can be found in [36] pp. 137–162. For the P-wave transducers (experiments 1–3), a combined sensitivity of c_P due to the uncertainties in diffraction correction, unwanted sidewall reflections in the acoustic experimental setup, repeatability, and sample length is estimated to less than 15 m/s using finite element simulations and reference measurements. The uncertainty contribution due to repeatability of the measurements is set to 11 m/s. By conducting measurements over several hours on a sample (without hydrate) placed within the pressure cell (Fig. 1), measurement results deviate less than 1 m/s. However, by conducting measurements and then decoupling and setting up the acoustic measurement setup again, measurements may deviate up to 11 m/s.

The absolute c_P is dependent on the repeatability of the measurements. During hydrate growth the transducers, buffers, and the sample are held in a fixed position and thus the repeatability of the change in c_P during hydrate growth is assumed to be much smaller than for absolute

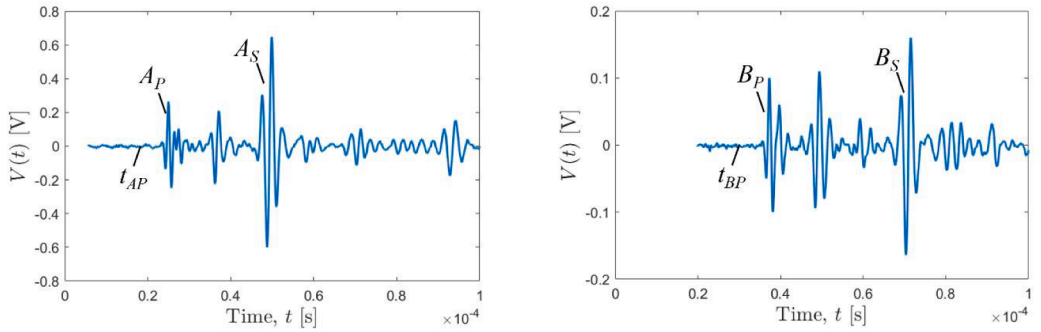

Fig. 2. Time traces for experiment 7 for $S_H \approx 0.4$. Events and first arrival transit times are shown for a) measurement A and b) measurement B.

measurements. This is clearly indicated by the repeatability measurements which change less than 1 m/s over time for a sample placed within the pressure cell. In general, measurements of the change in c_P are more accurate than the absolute c_P because hydrate growth in the core is assumed to have little or no effect on the listed uncertainty contributions, such as repeatability or sample length.

The sensitivity on c_P due to repeatability using S-wave transducers (experiments 4–8) is set to 45 m/s [36], however, the accuracy of the change in c_P during hydrate growth is assumed to be the same for the S and P-wave transducers.

3. Results

c_P was measured for eight Bentheim sandstone samples (see Table 1) with different S_{wi} during hydrate growth using the buffer rod measurement method and Fourier spectrum method at 500 kHz. First the baseline velocity (c_P before hydrate growth, $S_H = 0$) is presented, followed by measurements of experiments 1–8.

3.1. Baseline velocity

In Fig. 3, measurements (blue x-markers) and calculations (red plus markers and black circles) of the baseline velocity as a function of S_{wi} are presented for the eight sandstone samples (Table 1). The DEM [21] is used to calculate the stiffness of the dry Bentheim rock frame, and Gassmann's equation [16] to include fluid effects. The fluid effects are calculated in two different ways; "Uniform": a uniform distribution of water and gas in the pores, and "Patchy": the water and gas are distributed separately in the sandstone [19]. Such effective medium models have been used for decades to describe properties of porous materials [16,19,21] and thus not repeated here. The relatively good agreement between measurements and calculations gives confidence in the acoustic measurement results and provides some insight in the initial water/gas distribution before hydrate growth.

The material properties used in the calculations are given in Table 2. K_w, K_q, and K_g are the water, quartz, and methane gas bulk moduli, respectively. ρ_g, ρ_q, and ρ_w are the methane gas, quartz, and water densities, respectively. μ_q is the quartz shear moduli. The effective soft pore volume fraction, α_1, and volume fraction, v_1, are obtained from Wang et al. [48] by interpolating between the reported values for Bentheim sandstone. The stiff pore volume fraction is $v_2 = 1\text{-}v_1$ and the stiff pore aspect ratio, α_2, is set to 1, which is a typical value used for stiff pores [49,50] in sandstones. The porosities and initial water saturations from experiments 1–8 in Table 1 are used as input parameters.

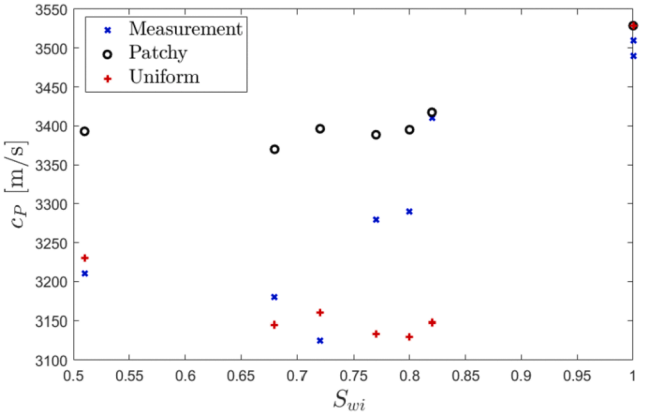

Fig. 3. Measurements (blue markers) and simulations of the baseline velocity ($S_H = 0$) for experiments 1–8. The gas/water fluid mixture is modeled to either have a uniform or a patchy distribution. (For interpretation of the references to colour in this figure legend, the reader is referred to the web version of this article.)

Table 2
List of material properties used in the simulations. K_g and ρ_q are calculated using the Peace Software [51] for temperature 4 °C and pressure 8.3 Mpa. The soft pore volume fraction, v_1, and soft pore aspect ratio, α_1, are obtained based on the values reported in [48]. The stiff pore aspect ratio, $\alpha_2 = 1$, is taken as one of the typical values in [49]. The rest of the parameters are taken from Waite et al. [4].

Parameter	Value	Reference
K_w	2.25 Gpa	[4]
K_q	36.6 Gpa	[4]
K_g	11 Mpa	[51]
ρ_g	70 kg/m^3	[51]
ρ_w	1000 kg/m^3	[4]
ρ_q	2650 kg/m^3	[4]
μ_q	45 Gpa	[4]
α_1	0,002	[48]
α_2	1	[49]
v_1	0,023	[48]

In Fig. 3, the deviation between measurements (blue) and simulations where gas and water are uniformly distributed is less than 50 m/s for the samples having $S_{wi} = 0.51$, 0.57, and 0.68. For the samples having $S_{wi} = 0.77$, 0.80, and 0.82, a patchy gas distribution gives the best agreement. By comparing the measurements and simulations, there seem to be a transition from uniform to partially patchy gas distribution at approximately $S_{wi} = 0.8$. For experiments 6, 7, and 8, where $S_{wi} = 0.82$, 1, and 1, respectively, a very good agreement is observed between the patchy distribution simulations and the measurements.

3.2. Change in c_p as a function of S_H for experiments with S_{wi} in the range 0.51–0.72

Fig. 4 shows the measurements during experiments 1, 2, and 3, where S_{wi} is 0.51, 0.68, and 0.72, respectively. In experiment 1 hydrates form quickly and c_P increases greatly with increasing S_H in the early stage of the hydrate formation process. The acoustic waveform is logged every 15 min and experiment 1 is thus better represented with markers than a continuous curve. (For experiments 2–8 the hydrate formation process is more slow and the datapoints are close enough to be represented with a continuous curve.) In experiment 1, c_P increases with approximately 800 m/s for S_H in the range 0–0.2, starting at c_P approximately 3200 m/s. For $S_H = 0.4 - 0.6$, c_P flattens out.

In experiments 2 and 3, S_{wi} is 0.68 and 0.72, respectively, and the baseline c_P is approximately 3110 m/s and 3180 m/s, respectively. The curves for experiment 2 and 3 show a similar increase in c_P for increasing S_H. For S_H in the range 0 – 0.1, little or no change is observed in c_P. A very small decline might be indicated in this range. For $S_H > 0.1$, a clear increase in c_P is observed. At $S_H = 0.5$ there is an increase of

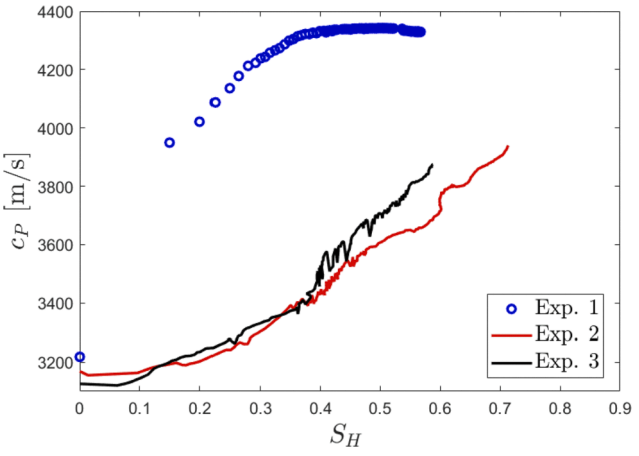

Fig. 4. Measured c_P as function of S_H for experiment 1 ($S_{wi} = 0.51$), experiment 2 ($S_{wi} = 0.68$), and experiment 3 ($S_{wi} = 0.72$).

approximately 450 m/s and 550 m/s relative to the baseline velocity, in experiments 2 and 3, respectively.

The sensitivity analysis detailed in section 2.4 indicates an uncertainty in c_P of 15 m/s for results presented in Fig. 4.

As described in [52], hydrates may be redistributed during the dynamic hydrate formation process. This may explain the ripples observed for the measured c_P in Fig. 4. Such ripples are observed for experiments 4–8 as well, shown in Figs. 5-6.

3.3. Change in c_p as a function of S_H for experiments with S_{wi} in the range 0.77–0.82

In Fig. 5, c_P is presented for experiments 4 ($S_{wi} = 0.77$), 5 ($S_{wi} = 0.80$), and 6 ($S_{wi} = 0.82$). Data is missing for S_H in the range 0.27 – 0.62 in experiment 5 due to a crash on the computer logging the acoustic waveforms. The computer was restarted the next day, however as Fig. 5 shows, important information of c_P during the hydrate formation process is missing. A new experiment was then immediately planned with approximately the same S_{wi} as experiment 5. This new experiment is in fact experiment 6. The existing data from experiment 5 still give useful information on the hydrate formation process for S_H less than 0.25 and is thus included in Fig. 5. The baseline c_P is approximately 3270 m/s in experiments 4 and 5, and 3400 m/s in experiment 6. In all three experiments there is some initial decline in the measured c_P for low S_H. After this decline, c_P increase and is measured to be higher than the baseline c_P from S_H approximately 0.1–0.15. The increase in c_P from the baseline velocity to $S_H = 0.5$ is approximately 500 m/s and 300 m/s, in experiments 4 and 6, respectively. For $S_H > 0.5$, the increase in c_P is higher for experiment 4 compared with experiment 6. The curve for experiment 5 flattens out and no change can be seen in the measured c_P for $S_H > 0.6$.

The sensitivity analysis detailed in section 2.4 indicates an uncertainty in c_P of 45 m/s for the results reported in Fig. 5. The change in c_P during hydrate growth, i.e relative to the baseline velocity is set to 15 m/s.

The measured baseline velocity ($S_H = 0$) in experiment 4 lies in between the "Uniform" and "Patchy" simulations in Fig. 3, indicating that there might be some regions in the sandstone having a patchy gas/water distribution.

The black curve for experiment 6 is approximately 100 m/s higher than for experiment 4 and 5. This may be partly explained by the slight difference in porosity (Table 1), between the cores in experiment 6, and experiments 4–5. Also, by comparing the simulated and measured baseline velocities in experiments 4–6 (Fig. 5), water and gas are indicated to be distributed in patches, especially in experiment 6. A patchy saturation will give a higher c_P than a uniform water/gas distribution.

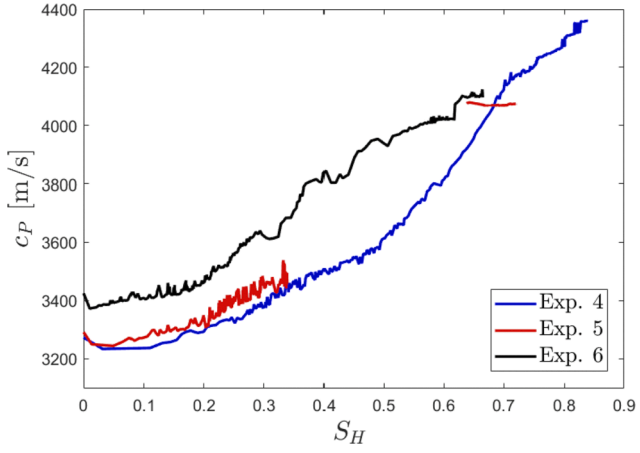

Fig. 5. Measured c_P as function of S_H for experiment 4 ($S_{wi} = 0.77$), experiment 5 ($S_{wi} = 0.80$), and experiment 6 ($S_{wi} = 0.82$).

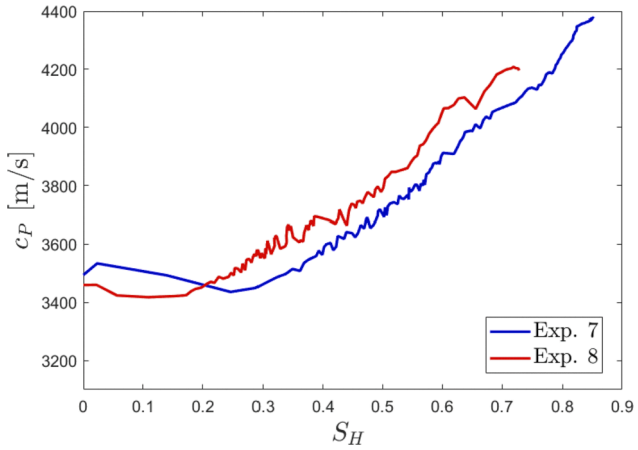

Fig. 6. Measured c_P as function of S_H for experiment 7 ($S_{wi} = 1$) experiment 8 ($S_{wi} = 1$).

3.4. Change in c_p as a function of S_H for experiments with fully water saturated samples

In Fig. 6, the measured c_P is presented for experiments 7 and 8, where $S_{wi} = 1$. The curves indicate an increase followed by a decrease in the measured c_P for low S_H. The "main" increase in c_P starts at S_H approximately 0.18 and 0.25 for experiments 7 and 8, respectively. The increase in c_P at $S_H = 0.5$ relative to the baseline is approximately 200 and 300 m/s in experiments 7 and 8, respectively.

As seen in Fig. 3, for $S_{wi} = 1$, the measured baseline c_P is lower than the simulated baseline c_P. This deviation might be explained if there are small amounts of gas still present in the pores, which is not accounted for in the simulations, where $S_{wi} = 1$.

The sensitivity analysis detailed in section 2.4 indicates an uncertainty in c_P of 45 m/s for the results reported in Fig. 6. The change in c_P during hydrate growth, i.e relative to the baseline velocity is set to 15 m/s.

3.5. Change in c_p as a function of S_{wi}

In Fig. 7, the change in c_P (relative to the baseline velocity) as a function of S_{wi} is presented for all experiments at a fixed hydrate saturation, in (a) $S_H = 0.5$ and (b) at $S_H = 0.25$. Fitting curves are also indicated in the figure. In (a), the data from experiment 5 ($S_{wi} = 0.8$) is missing due to a logging computer crash. The y-axis is labeled Δc_P, i.e the change in c_P relative to the baseline velocity for each of the experiments. It is evident that in the experiments where S_{wi} is lowest, the increase in c_P is highest. In experiment 1, where $S_{wi} = 0.51$, Δc_P is 1150 and 900 m/s at $S_H = 0.5$, and 0.25, respectively. At $S_H = 0.5$, for the experiments having S_{wi} in the range 0.68–0.82, Δc_P is in the range 300–600 m/s. For the same experiments, at $S_H = 0.25$, Δc_P is in the range 90–190 m/s. For experiments 7 and 8, where $S_{wi} = 1$, Δc_P is 200 and 300 m/s, respectively at $S_H = 0.5$. For these experiments, at $S_H = 0.25$, Δc_P is 20 and −50 m/s, respectively. The negative Δc_P comes from the decrease in the measured c_P reported in Fig. 6.

The sensitivity analysis detailed in section 2.4 indicates an uncertainty in the change in c_P of 15 m/s for the measurements presented in Fig. 7.

To highlight the decreasing tendency of Δc_P, fitting curves are included in Fig. 7. An exponential decreasing curve on the form $ae^{bS_{wi}}$ is found to give the best fit. In Fig. 7(a) the coefficients a and b describing the fitting curve are 6534 and −3.494, respectively, with an r-squared (R^2) value of 0.8791. In Fig. 7(b) the coefficients a and b describing the fitting curve are 78,130 and −8.768, respectively, with an R^2 value of 0.9579. The fitting curves are obtained with the function fit() in MATLAB version 2021a. The R^2 values are rather high, however, more

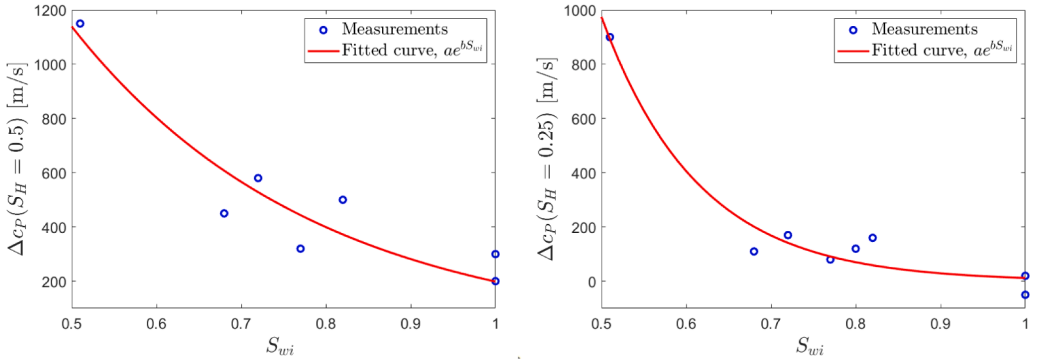

Fig. 7. The change in c_P (relative to the baseline velocity), Δc_P, as a function of S_{wi} is presented for all experiments at a fixed hydrate saturation. Fitting curves on the form $ae^{bS_{wi}}$ are indicated. (a) Δc_P at $S_H = 0.5$ with fitting curve coefficients a = 6534 and b = -3.494, and (b) Δc_P at $S_H = 0.25$ with with fitting curve coefficients a = 78130 and b = -8.768.

datapoints are needed to establish if such an exponential model is a good prediction of measurements reported on the form as shown in Fig. 7.

4. Discussion

For consolidated sediments, an increase in c_P during hydrate growth in the laboratory has been generally explained with hydrates taking part and stiffening the solid frame, whereas hydrates are assumed to be forming within the pore fluid if little or no change in c_P is observed [7,12,23]. The same overall relation between hydrate formation pattern and c_P is reported for unconsolidated hydrate bearing sediments [4–6,11,13].

In general, the DEM predicts a drastic increase in c_P of a porous material if the low aspect ratio pores a filled with a solid material such as hydrate [21]. By filling the higher aspect ratio pores, the DEM predicts a modest increase in c_P. Little or no change in c_P is predicted by the Gassmann's equation by letting hydrate act as a fluid.

As hydrates forming in the pore fluid is considered to have little effect on c_P, the increase in c_P observed in experiment 1 ($S_{wi} = 0.51$ in Fig. 4) is assumed to be caused by hydrates taking part in the solid frame. The measurements and calculations of the baseline velocity in Fig. 3, indicates that there is a uniform water/gas distribution for experiment 1. For such a distribution gas is at least partially available for lower aspect ratio pores and a portion of the hydrates will grow in these. Due to hydrophilic nature of sandstones, water will coat the pore walls for low S_{wi}. The hydrates will thus take part in the frame on the pore walls and not turn to a slurry mix of water and hydrate. This may explain the relatively rapid increase in c_P seen in experiment 1.

The results in experiments 2–8 are very different from experiment 1 in the sense that there is little change in c_P early in the hydrate formation process (Figs. 5-7). In Fig. 7 (b), this is clearly illustrated by the small change in c_P for S_H less than 0.25 for $S_{wi} \geq 0.68$. In (b), c_P tends to change less in the experiments with higher S_{wi}, indicating that hydrates form in the pore fluid when S_w is high. It has been argued that hydrate formation goes through two stages in water saturated pores; first a hydrate-water slurry stage and then a solidification stage [7]. This fits well with the results from experiments 2–8; After some initial stage of little change, c_P increase after a certain S_H in experiments 2–8. For higher S_{wi}, the water-hydrate slurry stage persists for a higher S_H compared with experiments with lower S_{wi}. More experiments could have been conducted in the S_{wi} range 0.51 – 0.68 to better describe the relation between cementing effects and hydrate formation. Such measurements could also add confidence in the tendency indicated by the fitting curves in Fig. 7.

In experiment 1, it was argued that some of the low aspect ratio pores were filled with hydrates from the very start of the hydrate formation process, leading to a clear increase in c_P. This can not be the case for experiments 2–8. Due to the capillary effect and the hydrophilic nature of sandstones drawing water into small pore spaces, it may seem viable that small aspect-ratio pores are fully water saturated. Thus, in experiments 2–6, hydrates may form at the water–gas interface in the larger pores with higher aspect ratios, giving a more modest increase in c_P.

Some unexpected results are observed in Figs. 5-6. There is a small decrease in c_P for low S_H in experiments 2–8. In experiment 7 in Fig. 6 there is also a short increase prior to this decrease for S_H approximately 0–0.025. Seemingly similar findings have been reported for shear wave measurements by Hu et al. [7], where a decrease of approximately 60 m/s in the shear wave velocity (c_S) was reported for S_H in the range 0 – 0.15. Such changes in c_P or c_S are not predicted by models for hydrates forming in the pore fluid. No explanation is provided in the current work for this change in c_P. It might be that free gas redistributes during the dynamic process of hydrate formation. Going from a patchy to a uniform or from a uniform to a patchy water/gas distribution (Fig. 3), may give a noticeable effect on c_P. Another potential explanation is that the volume expansion due to water forming into hydrate might cause small cracks in the sandstone, potentially softening the solid frame.

For an artificial consolidated porous ceramic material having $S_{wi} = 1.0$, hydrates were reported to form in the pore fluid for S_H less than 0.3 and form as part of the solid frame for $S_H > 0.3$ [7]. These findings are similar to the findings in the present work. Hydrates have been reported in general to act as cement in "gas-rich" systems where the gas is interconnected through the sample (low S_{wi}) [4] and hydrates grow at grain contact points. This trend is observed for experiment 1 ($S_{wi} = 0.51$), where hydrates seem to take part in the solid frame early in the hydrate formation process.

5. Conclusions

Measurements of the compressional wave phase velocity (c_P) are presented as a function of hydrate saturation, S_H, during hydrate growth for Bentheim sandstone. Eight experiments were conducted on eight sandstone samples, having initial water saturation, S_{wi}, in the range 0.51 – 1. It is discussed how S_{wi} relates to whether hydrates take part in the solid frame or form in the pore fluid during hydrate growth.

In the measurements, S_{wi} and S_H are observed to have a clear impact on the measured c_P. Early in the hydrate formation process in experiment 1, which has the lowest $S_{wi} = 0.51$, a clear increase in c_P as a function of S_H is observed. The differential effective medium theory, ascribe such an increase in c_P to cementing effects in the soft, low aspect-ratio pores. This cementing effect is assumed to be due to high gas availability when S_{wi} is low. In the other experiments 2–8, where $S_{wi} \geq 0.68$, there is a hydrate formation stage for low S_H where little or no change is observed in c_P. This is ascribed to hydrates forming in the pore

fluid by e.g. Gassmann's equation. For higher S_H a second hydrate formation stage follows where c_P increase for increasing S_H. Such a stage has been referred to by others as a "solidification stage" where hydrates residing in the pore fluid eventually start bridging the pores, increasing the stiffness of the rock. From the measurements reported in the current work, the S_H interval defining the first hydrate formation stage increase for increasing S_{wi}.

In previous studies on both consolidated and unconsolidated hydrate bearing sediments, hydrates have been reported to act as cement in "gas-rich" (low S_{wi}) systems and to form in the pore fluid in "water-rich" systems (high S_{wi}). This description of the hydrate morphology fits well with the results obtained in the current study, where c_P is studied for hydrate-bearing sandstone.

Declaration of Competing Interest

The authors declare that they have no known competing financial interests or personal relationships that could have appeared to influence the work reported in this paper.

Acknowledgments

This research is funded by the University of Bergen through a PhD scholarship of the first author. Thanks to Magne Vestrheim for important discussions, and other members of the Acoustics group, and the Petroleum and process technology group, at the Department of Physics and Technology, University of Bergen, Norway. Especially thanks to Roald Langøen for technical comments on the experimental setup and to Tor Arne Johansen for helping with numerical models.

Data availability

The measurement data used in the current study is published with open access at UiB Open Research Data, DataverseNO, https://doi.org/10.18710/GDT85X [41].

References

[1] Moridis GJ, Collett TS, Boswell R, Kurihara M, Reagan MT, Koh C, et al. Toward production from gas hydrates: Current status, assessment of resources, and simulation-based evaluation of technology and potential. SPE Reservoir Eval Eng 2009;12(05):745–71. https://doi.org/10.2118/114163-PA.

[2] Mienert J, Berndt C, Tréhu AM, Camerlenghi A, Liu C-S. World Atlas of Submarine Gas Hydrates in Continental Margins. Cham: Nature; 2022.

[3] Chand S, Minshull TA, Gei D, Carcione JM. Elastic velocity models for gas-hydrate-bearing sediments – A comparison. Geophys J Int 2004;159(2):573–90. https://doi.org/10.1111/j.1365-246X.2004.02387.x.

[4] Waite WF, Winters WJ, Mason DH. Methane hydrate formation in partially water-saturated Ottawa sand. Am Mineral 2004;89(8–9):1202–7. https://doi.org/10.2138/am-2004-8-906.

[5] Winters WJ, Pecher IA, Waite WF, Mason DH. Physical properties and rock physics models of sediment containing natural and laboratory-formed methane gas hydrate. Am Mineral 2004;89(8–9):1221–7. https://doi.org/10.2138/am-2004-8-909.

[6] Priest JA, Best AI, Clayton CRI. A laboratory investigation into the seismic velocities of methane gas hydrate-bearing sand. J Geophys Res Solid Earth 2005;110:B04102. https://doi.org/10.1029/2004JB003259.

[7] Guerin G, Goldberg D. Modeling of acoustic wave dissipation in gas hydrate-bearing sediments. Geochem Geophys Geosyst 2005;6(7):n/a–. https://doi.org/10.1029/2005GC000918.

[8] Hu GW, Ye YG, Zhang J, Liu CL, Diao SB, Wang JS. Acoustic properties of gas hydrate-bearing consolidated sediments and experimental testing of elastic velocity models. J Geophys Res 2010;115(B2):B02102. https://doi.org/10.1029/2008JB006160.

[9] Nakagawa S, Kneafsey T. Split Hopkinson resonant bar test and its application for seismic property characterization of geological media. In: Proc. Of 44th U.S. Rock mechanics symposium and 5th U.S.-Canada rock mechanics symposium, American Rock Mechanics Association, Salt Lake City, UT, June 27-30, 2010; 2010. p. 7.

[10] Rydzy, M. B., & Batzle, M. L. (2010). Ultrasonic velocities In laboratory-formed gas hydrate-bearing sediments. In Proc. Of 23rd EEGS Symposium on the Application of Geophysics to Engineering and Environmental Problems, Keystone, CO, April 11-15, 2010, 10 p.

[11] Zhang Q, Li F-G, Sun C-Y, Li Q-P, Wu X-Y, Liu B, et al. Compressional wave velocity measurements through sandy sediments containing methane hydrate. Am Mineral 2011;96(10):1425–32. https://doi.org/10.2138/am.2011.3681.

[12] Sahoo SK, Madhusudhan BN, Marín-Moreno H, North LJ, Ahmed S, Falcon-Suarez IH, et al. Laboratory insights into the effect of sediment-hosted methane hydrate morphology on elastic wave velocity from time-lapse 4-D synchrotron X-ray computed tomography. Geochem Geophys Geosyst 2018;19(11):4502–21. https://doi.org/10.1029/2018GC007710.

[13] Zhang Qi, Yang Z, He T, Lu H, Zhang Yi. Growth pattern of dispersed methane hydrates in brine- saturated unconsolidated sediments via joint velocity and resistivity analysis. J Nat Gas Sci Eng 2021;96:104279. https://doi.org/10.1016/j.jngse.2021.104279.

[14] Wei J, Wu T, Feng X, Liang J, Li W, Xie R, et al. Physical properties of gas hydrate-bearing pressure core sediments in the South China Sea. Geofluids 2021;2021:1–10. https://doi.org/10.1155/2021/6636125.

[15] Wang W, Ba J, Carcione JM, Liu X, Zhang L. Wave properties of gas-hydrate bearing sediments based on poroelasticity. Front Earth Sci 2021;9:283. https://doi.org/10.3389/feart.2021.640424.

[16] Gassmann F. Uber die Elastizitat poroser Medien. Vierteljahrsschrift Der Naturforschenden Gesellschaft in Zurich 1951;96:23 p.

[17] Marín-Moreno H, Sahoo SK, Best AI. Theoretical modeling insights into elastic wave attenuation mechanisms in marine sediments with pore-filling methane hydrate. J Geophys Res Solid Earth 2017;122(3):1835–47. https://doi.org/10.1002/2016JB013577.

[18] Zhang W, Liang J, Qiu H, Deng W, Meng M, He Y, et al. Double bottom simulating reflectors and tentative interpretation with implications for the dynamic accumulation of gas hydrates in the northern slope of the Qiongdongnan Basin, South China Sea. J Asian Earth Sci 2022;229:105151. https://doi.org/10.1016/j.jseaes.2022.105151.

[19] Helgerud MB, Dvorkin J, Nur A, Sakai A, Collett T. Elastic-wave velocity in marine sediments with gas hydrates: Effective medium modeling. Geophys Res Lett 1999;26(13):2021–4.

[20] Dvorkin J, Nur A, Yin H. Effective properties of cemented granular materials. Mech Mater 1994;18(4):351–66. https://doi.org/10.1016/0167-6636(94)90044-2.

[21] Norris AN. A differential scheme for the effective moduli of composites. Mech Mater 1985;4(1):1–16. https://doi.org/10.1016/0167-6636(85)90002-X.

[22] Zhang JJ, Bentley LR. Pore geometry and elastic moduli in sandstones. CREWES Res Rep 2003;15:1–20.

[23] Sadeq D, Alef K, Iglauer S, Lebedev M, Barifcani A. Compressional wave velocity of hydrate-bearing bentheimer sediments with varying pore fillings. Int J Hydrogen Energy 2018;43(52):23193–200. https://doi.org/10.1016/j.ijhydene.2018.10.169.

[24] Molyneux JB, Schmitt DR. Compressional-wave velocities in attenuating media: A laboratory physical model study. Geophysics 2000;65(4):1162–7. https://doi.org/10.1190/1.1444809.

[25] Sachse W, Pao Y. On the determination of phase and group velocities of dispersive waves in solids. J Appl Phys 1978;49(8):4320–7. https://doi.org/10.1063/1.325484.

[26] Duchkov AD, Duchkov AA, Permyakov ME, Manakov AY, Golikov NA, Drobchik AN. Acoustic properties of hydrate-bearing sand samples: laboratory measurements (setup, methods, and results). Russ Geol Geophys 2017;58(6):727–37. https://doi.org/10.1016/j.rgg.2016.09.029.

[27] Dugarov GA, Duchkov AA, Duchkov AD, Drobchik AN. Laboratory validation of effective acoustic velocity models for samples bearing hydrates of different type. J Nat Gas Sci Eng 2019;63:38–46. https://doi.org/10.1016/j.jngse.2019.01.007.

[28] Ding J, Cheng Y, Deng F, Yan C, Sun H, Li Q, et al. Experimental study on dynamic acoustic characteristics of natural gas hydrate sediments at different depths. Int J Hydrogen Energy 2020;45(51):26877–89. https://doi.org/10.1016/j.ijhydene.2020.06.295.

[29] Pearson C, Murphy J, Hermes R. Acoustic and resistivity measurements on rock samples containing tetrahydrofuran hydrates: Laboratory analogues to natural gas hydrate deposits. J Geophys Res Solid Earth 1986;91(B14):14132–8. https://doi.org/10.1029/JB091iB14p14132.

[30] Liu Z, Ning F, Hu G, Liu L, Liu C, Peng Li, et al. Characterization of seismic wave velocity and attenuation and interpretation of tetrahydrofuran hydrate-bearing sand using resonant column testing. Mar Pet Geol 2020;122:104620. https://doi.org/10.1016/j.marpetgeo.2020.104620.

[31] Lei L, Santamarina JC. Laboratory Strategies for Hydrate Formation in Fine-Grained Sediments. J Geophys Res Solid Earth 2018;123(4):2583–96. https://doi.org/10.1002/jgrb.v123.410.1002/2017JB014624.

[32] Ramstad T, Rueslåtten H. Pore scale numerical analysis for geological sequestration of CO2 (Technical Report TASK1. Trondheim, Norway: Numerical Rocks; 2013. p. 63.

[33] Ruedrich J, Siegesmund S. Salt and ice crystallisation in porous sandstones. Environ Geol 2007;52(2):225–49.

[34] Almenningen S. An experimental study of methane hydrates in sandstone cores (MSc thesis). Bergen, Norway: University of Bergen, Department of Physics and Technology; 2015.

[35] Almenningen S, Gauteplass J, Hauge LP, Barth T, Fernø MA, Ersland G. Measurements of CH4 and CO2 relative permeability in hydrate-bearing sandstone. J Petrol Sci Eng 2019;177:880–8.

[36] Sæther M. Elastic wave velocities and attenuation under methane hydrate growth in Bentheim sandstone. Measurements and modelling (PhD thesis). Bergen, Norway: University of Bergen, Department of Physics and Technology; 2018.

[37] Colorado School of Mines (2015). CSMGem. Software. http://hydrates.mines.edu/CHR/Software.html (Online accessed October 10, 2017).

[38] Almenningen S, Fotland P, Ersland G. Magnetic Resonance Imaging of Methane Hydrate Formation and Dissociation in Sandstone with Dual Water Saturation. Energies 2019;12(17):3231. https://doi.org/10.3390/en12173231.
[39] Ohmura R, Matsuda S, Uchida T, Ebinuma T, Narita H. Clathrate hydrate crystal growth in liquid water saturated with a guest substance: observations in a methane + water system. Cryst Growth Des 2005;5(3):953–7. https://doi.org/10.1021/cg049675u.
[40] Almenningen S, Flatlandsmo J, Fernø MA, Ersland G. Multiscale laboratory verification of depressurization for production of sedimentary methane hydrates. Soc Petrol Eng 2017;22(1):138–47. https://doi.org/10.2118/180015-PA.
[41] Sæther MM. Replication Data for: "Compressional wave phase velocity measurements during hydrate growth in partially and fully water saturated sandstone. DataverseNO https:// 2021. https://doi.org/10.18710/GDT85X.
[42] McSkimin HJ. Ultrasonic methods for measuring the mechanical properties of liquids and solids. In: Mason IWP, editor. Physical Acoustics: Principles and Methods, vol. 1. Muray Hill, NJ: Bell Telephone Laboratories Inc.; 1964. p. 271–334.
[43] Winkler KW, Plona TJ. Technique for measuring ultrasonic velocity and attenuation spectra in rocks under pressure. J Geophys Res Solid Earth 1982;87(B13):10776–80. https://doi.org/10.1029/JB087iB13p10776.
[44] Williams AO. The piston source at high frequencies. J Acoust Soc Am 1951;23(1):1–6. https://doi.org/10.1121/1.1906722.
[45] Rogers PH, Van Buren AL. An exact expression for the Lommel-diffraction correction integral. J Acoust Soc Am 1974;55(4):724–8. https://doi.org/10.1121/1.1914589.
[46] Tong J, Povey MJW. Pulse echo comparison method with FSUPER to measure velocity dispersion in n-tetradecane in water emulsions. Ultrasonics 2002;40(1):37–41. https://doi.org/10.1016/S0041-624X(02)00088-4.
[47] Treiber M, Kim J-Y, Jacobs LJ, Qu J. Correction for partial reflection in ultrasonic attenuation measurements using contact transducers. J Acoust Soc Am 2009;125(5):2946–53. https://doi.org/10.1121/1.3106125.
[48] Wang L, Rybacki E, Bonnelye A, Bohnhoff M, Dresen G. Experimental investigation on static and dynamic bulk moduli of dry and fluid-saturated porous sandstones. Rock Mech Rock Eng 2021;54(1):129–48. https://doi.org/10.1007/s00603-020-02248-3.
[49] Hong-Bing LI, Jia-Jia Z. A differential effective medium model of multiple-porosity rock and its analytical approximations for dry rock. Chin J Geophys 2014;57(6):835–45. https://doi.org/10.1002/cjg2.20146.
[50] Zhang L, Ba J, Fu L, Carcione JM, Cao C. Estimation of pore microstructure by using the static and dynamic moduli. Int J Rock Mech Min Sci 2019;113:24–30. https://doi.org/10.1016/j.ijrmms.2018.11.005.
[51] Wischnewski, B. (2007). Peace Software. Software. http://www.peacesoftware.de/ (Online accessed February 25, 2020).
[52] Hauge LP, Gauteplass J, Høyland MD, Ersland G, Kovscek A, Fernø MA. Pore-level hydrate formation mechanisms using realistic rock structures in high-pressure silicon micromodels. Int J Greenhouse Gas Control 2016;53:178–86. https://doi.org/10.1016/j.ijggc.2016.06.017.